

In Situ X-ray Absorption Spectroscopy of a Synergistic Co–Mn Oxide Catalyst for the Oxygen Reduction Reaction

Yao Yang,^{†,ID} Ying Wang,[‡] Yin Xiong,[†] Xin Huang,[§] Luxi Shen,[†] Rong Huang,^{||} Hongsen Wang,[†] James P. Pastore,[†] Seung-Ho Yu,^{‡,ID} Li Xiao,^{‡,ID} Joel D. Brock,[§] Lin Zhuang,^{*,‡,ID} and Héctor D. Abruña^{*,†,ID}

[†]Department of Chemistry and Chemical Biology, Baker Laboratory, Cornell University, Ithaca, New York 14853, United States

[‡]College of Chemistry and Molecular Sciences, Hubei Key Lab of Electrochemical Power Sources, and Institute for Advanced Studies, Wuhan University, Wuhan 430072, China

[§]School of Applied and Engineering Physics, Cornell University, Ithaca, New York 14853, United States

^{||}Cornell High Energy Synchrotron Source, Cornell University, Ithaca, New York 14853, United States

Supporting Information

ABSTRACT: Identifying the catalytically active site(s) in the oxygen reduction reaction (ORR), under real-time electrochemical conditions, is critical to the development of fuel cells and other technologies. We have employed *in situ* synchrotron-based X-ray absorption spectroscopy (XAS) to investigate the synergistic interaction of a Co–Mn oxide catalyst which exhibits impressive ORR activity in alkaline fuel cells. X-ray absorption near edge structure (XANES) was used to track the dynamic structural changes of Co and Mn under both steady state (constant applied potential) and nonsteady state (potentiodynamic cyclic voltammetry, CV). Under steady state conditions, both Mn and Co valences decreased at lower potentials, indicating the conversion from Mn(III,IV) and Co(III) to Mn(II,III) and Co(II), respectively. Rapid X-ray data acquisition, combined with a slow sweep rate in CV, enabled a 3 mV resolution in the applied potential, approaching a nonsteady (potentiodynamic) state. Changes in the Co and Mn valence states were simultaneous and exhibited periodic patterns that tracked the cyclic potential sweeps. To the best of our knowledge, this represents the first study, using *in situ* XAS, to resolve the synergistic catalytic mechanism of a bimetallic oxide. Strategies developed/described herein can provide a promising approach to unveil the reaction mechanism for other multimetallic electrocatalysts.

ORR using metal oxides remains unclear and catalysts, characterized *ex situ*, may not (and likely do not) maintain the same properties under real-time electrochemical conditions, which calls for the use of *in situ/operando* techniques to identify the true active site(s).

Synchrotron-based XAS is a powerful *in situ* technique to study electrocatalytic mechanisms because it can provide atomic-level information on electrochemical reactions. In addition, the high penetration of high-energy X-rays enables the *operando* study of electrochemical interfaces.¹⁰ *In situ* XAS has been used to study changes of precious metal-based ORR electrocatalysts.^{11–16} It has also been employed to follow the structural changes of manganese oxide,¹⁷ cobalt oxide¹⁸ and cobalt phosphate¹⁹ based materials for water oxidation. In this work, we demonstrate that Co–Mn oxide is a highly active electrocatalyst toward the ORR and, based on *in situ* XAS measurements, propose that Co and Mn serve as coactive/synergistic sites to catalyze the ORR.

Co–Mn oxide nanoparticles, supported on carbon, were synthesized via a hydrothermal method and their crystal structure was examined by X-ray diffraction (XRD) (Figure S1). $\text{Co}_3\text{O}_4/\text{C}$ and $\text{Mn}_3\text{O}_4/\text{C}$ were found to have cubic and tetragonal spinel structures, respectively. The synthesized $\text{Co}_{1.5}\text{Mn}_{1.5}\text{O}_4/\text{C}$ was verified to be single phase with a crystal structure similar to that of the cubic Co_3O_4 . The $\text{Co}_{1.5}\text{Mn}_{1.5}\text{O}_4/\text{C}$ exhibited very high ORR activity with a half-wave potential ($E_{1/2}$) of 0.85 V vs RHE, which compares very favorably with those of $\text{Co}_3\text{O}_4/\text{C}$ (0.76 V) and $\text{Mn}_3\text{O}_4/\text{C}$ (0.77 V) (Figure S2A). $\text{Co}_{1.5}\text{Mn}_{1.5}\text{O}_4/\text{C}$ had a mass-specific activity (MA) of 28.41 A/g at 0.85 V, five times higher than that of $\text{Mn}_3\text{O}_4/\text{C}$ and ten times higher than that of $\text{Mn}_3\text{O}_4/\text{C}$ (Figure S2B). The superior ORR activity of the bimetallic $\text{Co}_{1.5}\text{Mn}_{1.5}\text{O}_4/\text{C}$, over monometallic $\text{Co}_3\text{O}_4/\text{C}$ and $\text{Mn}_3\text{O}_4/\text{C}$, suggests an underlying synergistic catalytic mechanism involving both Co and Mn to catalyze the reduction of oxygen.

Synchrotron-based XAS was employed to investigate the catalytic mechanism of $\text{Co}_{1.5}\text{Mn}_{1.5}\text{O}_4/\text{C}$ under real-time *operando* electrochemical conditions. We designed a new

As high-efficiency energy-conversion devices, proton exchange membrane fuel cells (PEMFCs) have been recognized as critical technologies for electric vehicles.^{1,2} However, PEMFCs rely on expensive Pt-based electrocatalysts for the sluggish ORR.^{3–6} As an emerging alternative, alkaline fuel cells have drawn increasing attention since they enable the use of nonprecious metal electrocatalysts.^{7,8} To facilitate the ORR in alkaline media, great efforts have been devoted to the search of alternative electrocatalysts. Among these, 3d metal oxides have garnered increasing interest as a novel family as ORR electrocatalysts due to their high activity, long durability and low cost.⁹ However, the electrocatalytic mechanism of the

Received: November 24, 2018

Published: January 15, 2019

electrochemical cell for *in situ* XAS measurements, made of chemically inert Teflon and in which the thickness of the electrolyte could be controlled to be less than 200 μm (Figures 1 and S3). The working electrode (WE) consisted of a 40 μm

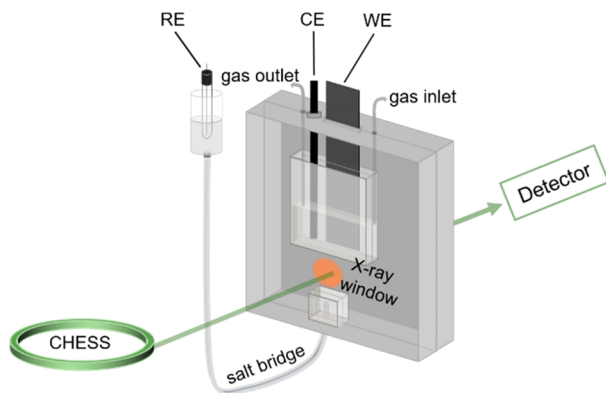


Figure 1. Schematic of the *in situ* XAS electrochemical cell. Working electrode (WE, catalyst on carbon paper) and counter electrode (CE, carbon rod) were immersed in 1 M KOH solution. The reference electrode was connected to the cell by a salt bridge to minimize IR drops caused by the resistance in the thin electrolyte layer (<200 μm) within the X-ray window.

catalyst layer sprayed/deposited on 200 μm thick carbon paper (Figure S4). Prior to the *in situ* XAS measurements, a CV of the $\text{Co}_{1.5}\text{Mn}_{1.5}\text{O}_4/\text{C}$ electrode was carried out in both the *in situ* XAS homemade cell and a conventional electrochemical cell, to verify that the *in situ* cell exhibited the characteristic redox couples of the Co–Mn oxide (Figure S5). The CVs of the electrocatalysts were then tested with the X-ray beam on and off revealing no noticeable beam damage (Figure S6), indicating that studies of the electrocatalytic mechanism would not be affected by the X-ray beam during *in situ* X-ray experiments.

To investigate the steady-state electrochemical response of the Co–Mn oxide catalysts, the applied potential was held constant while *in situ* XANES spectra were acquired, after the current had dropped to background levels. Based on the CV response of the catalysts at a sweep rate of 1 mV/s (Figure S6), constant applied potentials of 0.95, 1.15 and 0.75 V corresponding to the oxidation peak and potentials before and after the peak, respectively, were applied. Similarly, potentials of 0.55, 0.75 and 0.4 V corresponding to the reduction peak and potentials before and after the peak, respectively, were applied. The XANES spectra around the Mn K-edge exhibited systematic changes in the local electronic structure of $\text{Co}_{1.5}\text{Mn}_{1.5}\text{O}_4$ (Figure 2). The magnified inset on the left of the shoulder peak at 6553 eV showed a gradual increase in the peak intensity and a small shift to lower energies when the applied potential decreased from 1.15 to 0.4 V, indicating a lower Mn valence at the more negative potentials. The most intense peak, near 6559 eV, originates from an electronic transition from 1s to 4p orbitals. In the pre-edge region, the peak at 6540 eV arises from the transition from 1s to 3d orbitals. Although 1s-3d transitions are generally not allowed, due to the dipole selection rule, it can be observed if the absorber coordinates in a noncentrosymmetric geometry, allowing for the hybridization of d and p orbitals, indicating that the MnO_6 octahedra are slightly Jahn–Teller distorted.

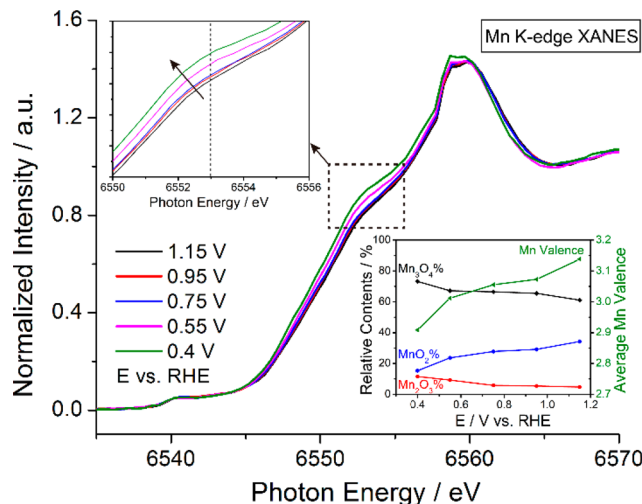


Figure 2. *In situ* XANES spectra of the Mn K-edge at a series of applied potentials. Top left inset shows an expanded section from 6550 to 6556 eV. The lower right inset shows the result of the Mn valence analysis by using the linear combination fitting (LCF) method and Mn_3O_4 (II,III), Mn_2O_3 (III) and MnO_2 (IV) as references.

In order to quantitatively study the Mn valence changes, we used the linear combination fitting (LCF) method with reference manganese oxides including MnO (II), Mn_3O_4 (II,III), Mn_2O_3 (III) and MnO_2 (IV). As shown in Figure S7, the LCF is able to fit well the experimental Mn XANES spectra and allows calculating the relative contributions in terms of the different Mn oxide references. As shown in the lower right inset of Figure 2, when the applied potential decreases from 1.15 to 0.4 V, the $\text{MnO}_2\%$ contribution decreases by 19% while $\text{Mn}_3\text{O}_4\%$ and $\text{Mn}_2\text{O}_3\%$ increase by 12% and 7%, respectively. $\text{MnO}\%$ was calculated to be 0% at essentially all potentials. Overall, the average Mn valence decreases from 3.15 to 2.91. This systematic valence conversion of Mn(III,IV) to Mn(II,III) indicates that various Mn species can serve as the active site to catalyze the ORR.

Similar to changes in the Mn valence at a series of applied potentials, XANES spectra, around the Co K-edge, also show regular changes in the local electronic structure of Co atoms in $\text{Co}_{1.5}\text{Mn}_{1.5}\text{O}_4/\text{C}$ (Figure 3). The magnified inset (top left) of Co XANES spectra around 7722.5 eV reveals a gradual increase in the peak intensity and a small shift to lower energies when the applied potential decreased from 1.15 to 0.4 V, indicating a lower Co valence at lower applied potentials. LCF was also employed to quantitatively analyze the Co valence with $\text{Co}(\text{OH})_2$ (II), Co_3O_4 (II,III) and CoOOH (III) as cobalt oxide references (Figure S8). When the applied potential was varied from 1.1 to 0.4 V, the CoOOH contribution decreased by 14% while that of $\text{Co}(\text{OH})_2$ increased by 19%. In contrast to changes for $\text{Mn}_3\text{O}_4\%$, the $\text{Co}_3\text{O}_4\%$ remained relatively stable at the different applied potentials. Overall, the average Co valence decreased from 2.75 to 2.57, indicating a valence conversion from Co(III) to Co(II). Since the Co valence changes with the applied potential took place at the same time as Mn, it suggests that Co and Mn could serve as coactive sites to catalyze the ORR.

While Co and Mn valence changes could be monitored under steady state, it would be much more valuable if we could also track the dynamic valence changes of Co and Mn at the same time under nonsteady conditions. However, a typical

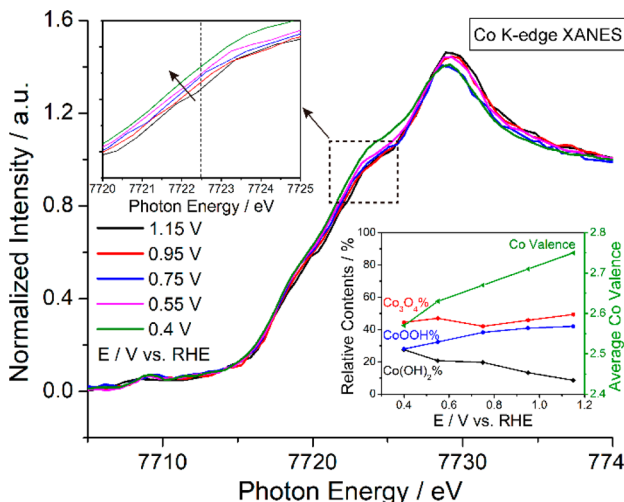


Figure 3. *In situ* XANES spectra of the Co K-edge at a series of applied potentials. Top left inset shows an expanded section from 7720 to 7725 eV. The lower right inset shows the result of the Co valence analysis, using the LCF method with $\text{Co}(\text{OH})_2$ (II), Co_3O_4 (II,III) and CoOOH (III) as references.

high-quality XANES spectrum takes 20–30 min to acquire, making it impossible to acquire one XANES spectrum while the potential is being scanned in a CV. Alternatively, characteristic photon energy values corresponding to the Co and Mn valence changes could be used as probes to track the dynamic valence changes during a CV scan. Co and Mn XANES at 7722.5 and 6553.0 eV, respectively, were used as the characteristic energy values where the largest changes in the X-ray intensities, with applied potential, occurred. In order to quantify the speed at which a nonsteady state could be tracked, a new concept, “electrode potential resolution”, was defined as the potential interval over which a single X-ray data point could be acquired. In this work, the electrode potential resolution = potential sweep rate \times X-ray acquisition time = 1 mV/s \times 3 s = 3 mV, meaning that the X-ray signal is averaged over a 3 mV potential interval, closely approximating a nonsteady (potentiodynamic) measurement. We divided the cyclic voltammogram into two regions, based on the sign of the current (upper inset of Figure 4). The positive current from 0.42 to 1.25 V and from 1.25 to 0.42 V (clockwise) indicates oxidation/reduction currents where Mn and Co are converted into higher/lower valence species, respectively.

As shown in Figure 4, the relative X-ray intensities of Co and Mn changed with the same periodic pattern as the cyclic potential sweep. The relative X-ray intensity was calculated by $\ln(I_1/I_2)$ where I_1 and I_2 are the incident and transmitted X-ray beam intensities, respectively. When the electrode potential was scanned from the upper limit (1.4 V) to the lower limit (0.3 V) (reductive current), the relative X-ray intensities evolved from minimum (higher Co, Mn valence) to maximum values (lower Co, Mn valence), indicating that $\text{Co}_{1.5}\text{Mn}_{1.5}\text{O}_4$ is reduced with Co(III) being converted into Co(II) and Mn(III,IV) being converted into Mn(II,III). Co(II) and Mn(II,III) reach their maxima at 0.42 V, instead of at the lower potential limit (0.3 V), while Co(III) and Mn(III,IV) reach their maxima at 1.25 V, instead of at the higher potential limit (1.4 V). This is fully consistent with the boundary potentials (0.42, 1.25 V) of oxidation and reduction currents in the CV. The periodic patterns of Co and Mn valence changes

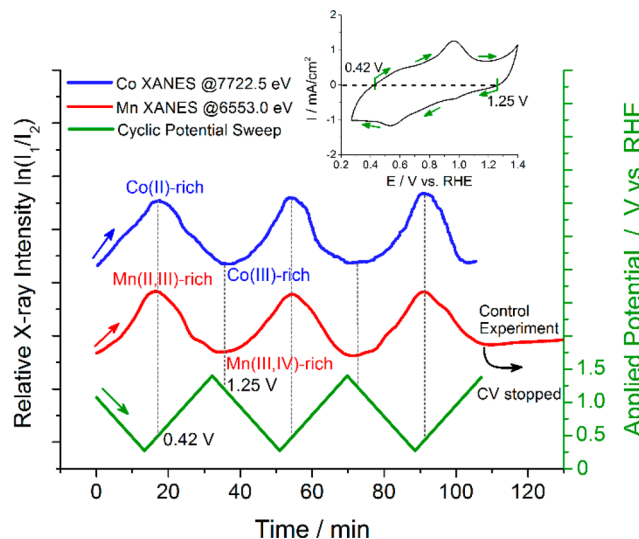


Figure 4. Periodic changes in the relative X-ray intensities ($\ln(I_1/I_2)$) at 7722.5 eV (Co K-edge) and 6553.0 eV (Mn K-edge) as a function of the cyclic potential sweep. Intensity variations at 7722.5 and 6553.0 eV reflect the conversion between Co(II) and Co(III), Mn(II,III) and Mn(IV), respectively. The upper inset shows the corresponding CV at 1 mV/s over the potential range of 0.3–1.4 V vs RHE. Oxidation and reduction currents in the CV are divided by two boundary potentials, 0.42 and 1.25 V, respectively.

are in sync with each other, strongly suggesting a synergistic catalysis mechanism between Co and Mn toward the ORR. Furthermore, dynamic changes in the Co and Mn valences were reproducible over the time period of 2 h, indicating that the catalyst is stable within the experimental time scale. To rigorously evaluate the effect(s) of the applied cyclic potential sweep, a control experiment was performed by acquiring the X-ray signal over the Mn XANES region without an applied potential. The fact that there were no changes in the X-ray intensity indicates that the dynamic changes of Co and Mn valences primarily arise from the applied potential sweep, and not from X-ray-generated photoelectrons.

In conclusion, *in situ* X-ray absorption spectroscopy (XAS) has been employed to identify the active sites of a bimetallic $\text{Co}_{1.5}\text{Mn}_{1.5}\text{O}_4/\text{C}$ catalyst, which exhibits impressive activity toward the ORR. We used *in situ* XANES to track the oxidation state changes of Co and Mn not only under a constant applied potential but also during dynamic cyclic voltammetry. The periodic conversion between Mn(III,IV), Co(III) and Mn(II,III), Co(II) during the CV indicates that $\text{Co}^{2+/-3}$ and $\text{Mn}^{2+/-3/4}$ redox couples could serve as coactive sites to synergistically catalyze the ORR.

ASSOCIATED CONTENT

S Supporting Information

The Supporting Information is available free of charge on the ACS Publications website at DOI: 10.1021/jacs.8b12243.

Synthesis, structural characterizations of XRD, TEM and *in situ* XAS, electrochemical tests of RDE and APEFC, design details of the homemade device and the CV profiles, LCF valence analysis, including Figures S1–S8 (PDF)

■ AUTHOR INFORMATION**Corresponding Authors***hda1@cornell.edu*lzhuang@whu.edu.cn**ORCID** ®Yao Yang: [0000-0003-0321-3792](https://orcid.org/0000-0003-0321-3792)Seung-Ho Yu: [0000-0003-4833-3181](https://orcid.org/0000-0003-4833-3181)Li Xiao: [0000-0002-6416-3138](https://orcid.org/0000-0002-6416-3138)Lin Zhuang: [0000-0002-5642-6735](https://orcid.org/0000-0002-5642-6735)Héctor D. Abruña: [0000-0002-3948-356X](https://orcid.org/0000-0002-3948-356X)**Notes**

The authors declare no competing financial interest.

■ ACKNOWLEDGMENTS

This work was supported as part of the Center for Alkaline Based Energy Solutions (CABES) an Energy Frontier Research Center funded by the U.S. Department of Energy, Office of Science, Office of Basic Energy Sciences, under Award No. DESC0019445. This work is based upon research conducted at the Cornell High Energy Synchrotron Source (CHESS) which is supported by the National Science Foundation under award DMR-1332208. This work made use of SEM/TEM facilities of the Cornell Center for Materials Research (CCMR), which are supported through the National Science Foundation Materials Research Science and Engineering Center (NSF MRSEC) program (DMR-1719875). This work was also financially supported by the National Natural Science Foundation of China (21872108, 91545205). We appreciate the assistance with the device fabrication from Stephan Felix and Chris Cowulich from the machine shop in the Laboratory of Atomic and Solid State Physics (LASSP) at Cornell University. We are grateful to Xinran Feng at Cornell University for the help with XANES data analysis. We acknowledge the help from Dr. Xiaoming Wang and Prof. Yoshiharu Uchimoto at Kyoto University for some synchrotron tests. We also thank Wei Liu at Wuhan University for his help with powder XRD measurements.

■ REFERENCES

- (1) Debe, M. K. Electrocatalyst Approaches and Challenges for Automotive Fuel Cells. *Nature* **2012**, *486*, 43–51.
- (2) Gasteiger, H. A.; Kocha, S. S.; Sompalli, B.; Wagner, F. T. Activity Benchmarks and Requirements for Pt, Pt-alloy, and non-Pt Oxygen Reduction Catalysts for PEMFCs. *Appl. Catal., B* **2005**, *56*, 9–35.
- (3) Xiong, Y.; Yang, Y.; DiSalvo, F. J.; Abruña, H. D. Pt-Decorated Composition-Tunable Pd–Fe@Pd/C Core–Shell Nanoparticles with Enhanced Electrocatalytic Activity toward the Oxygen Reduction Reaction. *J. Am. Chem. Soc.* **2018**, *140*, 7248–7255.
- (4) Wang, G.; Huang, B.; Xiao, L.; Ren, Z.; Chen, H.; Wang, D.; Abruña, H. D.; Lu, J.; Zhuang, L. Pt Skin on AuCu Intermetallic Substrate: A Strategy to Maximize Pt Utilization for Fuel Cells. *J. Am. Chem. Soc.* **2014**, *136*, 9643–9649.
- (5) Wang, D.; Xin, H. L.; Hovden, R.; Wang, H.; Yu, Y.; Muller, D. A.; DiSalvo, F. J.; Abruña, H. D. Structurally Ordered Intermetallic Platinum–Cobalt Core–Shell Nanoparticles with Enhanced Activity and Stability as Oxygen Reduction Electrocatalysts. *Nat. Mater.* **2013**, *12*, 81–87.
- (6) Shao, M.; Chang, Q.; Dodelet, J.; Chenitz, R. Recent Advances in Electrocatalysts for Oxygen Reduction Reaction. *Chem. Rev.* **2016**, *116*, 3594–3657.
- (7) Lu, S.; Pan, J.; Huang, A.; Zhuang, L.; Lu, J. Alkaline Polymer Electrolyte Fuel Cells Completely Free from Noble Metal Catalysts. *Proc. Natl. Acad. Sci. U. S. A.* **2008**, *105*, 20611–20614.
- (8) Pan, J.; Chen, C.; Zhuang, L.; Lu, J. Designing Advanced Alkaline Polymer Electrolytes for Fuel Cell Applications. *Acc. Chem. Res.* **2012**, *45*, 473.
- (9) Ge, X.; Sumboja, A.; Wuu, D.; An, T.; Li, B.; Goh, F. W. T.; Hor, T. S. A.; Zong, Y.; Liu, Z. Oxygen Reduction in Alkaline Media: From Mechanisms to Recent Advances of Catalysts. *ACS Catal.* **2015**, *5*, 4643–4667.
- (10) Abruña, H. D. *Electrochemical Interface: Modern Techniques for In Situ Interface Characterization*; VCH: New York, 1991.
- (11) Mukerjee, S.; Srinivasan, S.; Soriaga, M. P.; McBreen, J. Role of Structural and Electronic Properties of Pt and Pt Alloys on Electrocatalysts of Oxygen Reduction. *J. Electrochem. Soc.* **1995**, *142*, 1409–1421.
- (12) Becknell, N.; Kang, Y.; Chen, C.; Resasco, J.; Kornienko, N.; Guo, J.; Markovic, N. M.; Somorjai, G. A.; Stamenkovic, V. R.; Yang, P. Atomic Structure of Pt₃Ni Nanoframe Electrocatalysts by In Situ X-ray Absorption Spectroscopy. *J. Am. Chem. Soc.* **2015**, *137*, 15817–15824.
- (13) Friebel, D.; Viswanathan, V.; Miller, D.; Anniyev, T.; Ogasawara, H.; Larsen, A. H.; O’Grady, C. P.; Nørskov, J. K.; Nilsson, A. Balance of Nanostructure and Bimetallic Interactions in Pt Model Fuel Cell Catalysts: In Situ XAS and DFT Study. *J. Am. Chem. Soc.* **2012**, *134*, 9664–9671.
- (14) Erickson, E. M.; Thorum, M. S.; Vasić, R.; Marinković, N. S.; Frenkel, A. I.; Gewirth, A. A.; Nuzzo, R. G. In Situ Electrochemical X-ray Absorption Spectroscopy of Oxygen Reduction Electrocatalysis with High Oxygen Flux. *J. Am. Chem. Soc.* **2012**, *134*, 197–200.
- (15) Imai, H.; Izumi, K.; Matsumoto, M.; Kubo, Y.; Kato, K.; Imai, Y. In Situ and Real-Time Monitoring of Oxide Growth in a Few Monolayers at Surfaces of Platinum Nanoparticles in Aqueous Media. *J. Am. Chem. Soc.* **2009**, *131*, 6293–6300.
- (16) Casalongue, H. S.; Kaya, S.; Viswanathan, V.; Miller, D. J.; Friebel, D.; Hansen, H. A.; Nørskov, J. K.; Nilsson, A.; Ogasawara, H. Direct Observation of the Oxygenerated Species during Oxygen Reduction on a Platinum Fuel Cell Cathode. *Nat. Commun.* **2013**, *4*, 2817.
- (17) Gorlin, Y.; Lassalle-Kaiser, B.; Benck, J. D.; Gul, S.; Webb, S. M.; Yachandra, V. K.; Yano, J.; Jaramillo, T. F. In Situ X-ray Absorption Spectroscopy Investigation of a Bifunctional Manganese Oxide Catalyst with High Activity for Electrochemical Water Oxidation and Oxygen Reduction. *J. Am. Chem. Soc.* **2013**, *135*, 8525–8534.
- (18) Risch, M.; Ringleb, F.; Kohlhoff, M.; Bogdanoff, P.; Chernev, P.; Zaharieva, I.; Dau, H. Water Oxidation by Amorphous Cobalt-Based Oxides: In situ Tracking of Redox Transitions and Mode of Catalysis. *Energy Environ. Sci.* **2015**, *8*, 661.
- (19) Kanan, M. W.; Yano, J.; Surendranath, Y.; Dincă, M.; Yachandra, V. K.; Nocera, D. G. Structure and Valency of a Cobalt–Phosphate Water Oxidation Catalyst Determined by In Situ X-ray Spectroscopy. *J. Am. Chem. Soc.* **2010**, *132*, 13692–13701.